Check for updates

# Ultra-High-Speed Laser Cladding of Stellite® 6 Alloy on Mild Steel

ZEFENG WU,[1,3] MA QIAN [ID],[1,3,4] MILAN BRANDT,[1,3]
and NEIL MATTHEWS[2,3]

1.—Centre for Additive Manufacturing, School of Engineering, RMIT University, Melbourne, VIC 3000, Australia. 2.—RUAG Australia, Pty Ltd., 836 Mountain Hwy, Bayswater, VIC 3153, Australia. 3.—The Australian Research Council (ARC) Industrial Transformation Training Centre in Surface Engineering for Advanced Materials (SEAM), Hawthorn, Australia. 4.—e-mail: ma.qian@rmit.edu.au

Ultra-high-speed laser cladding, which refers to metal deposition at speeds > 20 m/min or rates of 120 cm$^2$/min, is an emerging technique that extends the conventional laser cladding process envelope without compromising the coating quality. This research investigates the effects of the laser energy density (2.56–15.00 J/mm$^2$) and powder stream focal position relative to the substrate (0.2–0.8 mm) on the clad layer thickness and as-deposited microstructure of Stellite® 6 coating on mild steel substrate. The laser energy density was found to be the dictating factor affecting the coating thickness, chemical composition, as-deposited microstructure, and overall coating quality. The powder stream focal position above the substrate surface determined the heated powder volume above the substrate, leading to increased coating thickness. The clad layer thickness can be controlled via changing the laser energy density and powder stream focal position.

## INTRODUCTION

Laser cladding (LC) refers to the deposition of a powder or wire material on the surface of another material with a single laser beam or even multi-laser beams for a wide variety of purposes, including repair, re-manufacturing, or novel surface properties. The powder or wire feedstock is delivered to the melt pool created by the laser beam, which solidifies after the laser beam moves away.[1] The rapid solidification during LC produces a much more refined microstructure in the coating or deposited alloy, which in general leads to its improved mechanical performance, compared with those fabricated by traditional manufacturing technologies such as gas tungsten arc welding.[2] The developments in LC technology and feedstock materials in the last 2 decades have enabled it to become an industrially accepted process. A variety of industry sectors such as the aviation, automotive, shipbuilding, power generation and oil and gas have adopted the process for repair and refurbishment of components and more recently additive manufacture. The technology has been used to deposit a vast array of different materials, including ceramics and composite materials, on various metallic surfaces.[1,3]

Ultra-high-speed laser cladding (UHSLC) is a recent development as a next-generation laser cladding technology.[4,5] It produces dense layers at the micron scale (50–250 $\mu$m) with minimal dilution of cladding materials by the substrate.[4–6] The process involves focusing a powder stream above the cladding surface at a distance between 0.2 mm and 3 mm during material deposition, allowing the powder material to be heated and partially melted by the laser beam, which typically has a laser spot size between 0.8 mm and 1.5 mm, before entering the melt pool on the substrate surface.[4,5] The elevated powder stream focal position is regarded as the critical feature or contributing factor that has enabled UHSLC, compared with conventional LC, which operates typically up to 2 m/min.[4–6] The grain refinement effect from the rapid solidification process of UHSLC improves the wear and corrosion resistance of the deposited material,[7–9] in addition

(Published online October 15, 2020)

to improving the economic feasibility of component repairs and hardfacing for large mechanical equipment at remote operation sites.[10,11]

Stellite® 6 is a cobalt-based alloy (Table I) with high-temperature wear and corrosion resistance. It has been widely used for surface protection on metallic components.[10,11] A recent study on the UHSLC of Stellite® 6 demonstrated a clear improvement in its wear resistance due to increased microhardness.[5] Crack initiation however occurred during deposition at ultrahigh process speeds (e.g., 50 m/min), caused by high residual stress in the deposited layers. No cracking was observed when the process speed was reduced to 20 m/min while maintaining the focused powder stream position. To date, limited information is available on the effect of process variables, especially the focused powder stream position on the as-deposited characteristics of Stellite® 6 coatings at high speed. This study fills this knowledge gap and provides new experimental details on UHSLC of Stellite® 6 powder.

## EXPERIMENTAL METHODOLOGY

### Materials, Experimental Set-Up, and Deposition Parameters

UHSLC was carried out on a TRUMPF TruLaser Cell 7020 system (TRUMPF Group) equipped with a 3.0-kW disk laser and a coaxial laser cladding head with a focal length of 200 mm and powder stream focal length of 10 mm (Fig. 1a). A 200-mm-long mild steel tube substrate with an outer diameter of 60 mm and wall thickness of 4 mm was set up in a rotary chuck that is integrated in, and controlled by, the TruLaser Cell 7020 system. The laser processing speed on the substrate surface was determined via the angular speed of the rotary chuck and the cross-sectional radius of the substrate. The Stellite® 6 powder (Table I and Fig. 1b) from Deloro Wear Solution GmbH had a particle size distribution in the range 50–100 $\mu$m to conform to the requirements of the cladding head.

The cladding was carried out at processing speeds from 10 m/min to 30 m/min while the powder focus position was varied from 0.2 mm to 0.8 mm (Table I). The geometric positions of the laser beam and powder stream are illustrated in Fig. 1c with a schematic in Fig. 1d on how the continuously operating laser beam travels on the substrate surface during deposition. The co-axial nozzle and the laser optic are continuously moving in the nozzle moving direction in Fig. 1a while the substrate rotates independently to the laser beam. Therefore, the laser beam spot travels in a spring-like or helical pattern relative to the cladding surface (Fig. 1d). The laser energy density, $E_l$, is used in the study to reflect the collective influence of laser power, $P$, laser process speed, $V_l$, and laser spot diameter, $D_l$,[12–14] based on Eq. 1.

$$E_l = \frac{P}{D_l V_l} \qquad (1)$$

The acceleration and deceleration of the rotary chuck at the beginning and the end of deposition were found to vary with the laser processing speed. Therefore, each deposition was carried out with three rotations to mitigate this variation and to reach the targeted speed value (10 m/min, 20 m/min, and 30 m/min) in the middle region of the clad samples.

Each clad track corresponds to a unique combination of process variables listed in Table II. A Phantom V1610 high-speed monochrome camera (Vision Research Inc.) was used to capture the powder particle distribution at 1000 frames per second before UHSLC deposition.

This study employed a fixed powder mass flow rate of 15 g/min. The argon shielding gas and helium carrier gas were set at 16 L/min and 10 L/min, respectively. The analysis of the co-axial powder particle distribution, shown in Fig. 2, uses the images captured from the high-speed camera and the open-source ImageJ software to determine the characteristics of the powder stream. Assuming the powder stream is symmetrical about the Z axis of the laser beam as well as the powder stream focal plane (Fig. 1c), the half divergence angle of the powder stream and the powder stream focus diameter were measured to be $20.4° \pm 0.2°$ and $1.1$ mm $\pm 0.1$ mm, respectively. It is worth noting that the powder stream characteristics in this study were measured from two-dimensional (2D) images. In the future, the particle motion and velocity in the 3D space should be determined, including the powder mass flow rate, number of particles in the area of interest, particle size distribution, and position displacements of the tracking particles.[6] The laser beam characteristics were collected from the focus line calibration data on the Trumpf TruLaser Cell® 7020 system. The laser beam operates with a Gaussian profile. The half-divergence angle of the laser beam and the laser focal spot diameter were 1.44° and 0.614 mm, respectively, in this study.

**Table I. Chemical compositions of Stellite® 6 powder and mild steel substrate**

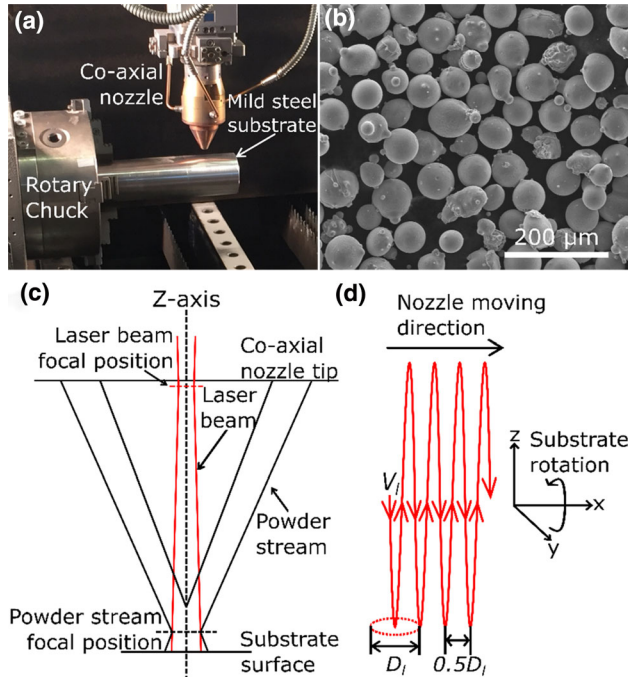| Element (wt.%) | Co | Cr | W | C | Ni | Mo | Fe | Si | P | S | Others |
|---|---|---|---|---|---|---|---|---|---|---|---|
| Stellite® 6 | Bal. | 29 | 4.5 | 1.1 | < 2.0 | < 1.0 | < 2.0 | < 2.0 | – | – | < 1.0 |
| Mild steel | – | – | – | 0.2 | – | – | Bal. | < 0.4 | 0.04 | 0.05 | – |

Fig. 1. (a) Experimental set-up of the UHSLC deposition. (b) The Stellite® 6 powder. (c) The geometric positions of both the laser beam and the defocused powder stream. (d) Illustration of a continuously operating laser beam during deposition in a helical pattern relative to the substrate at a laser process speed, $V_l$, a laser spot diameter, $D_l$, and a 50% track overlap in the study.
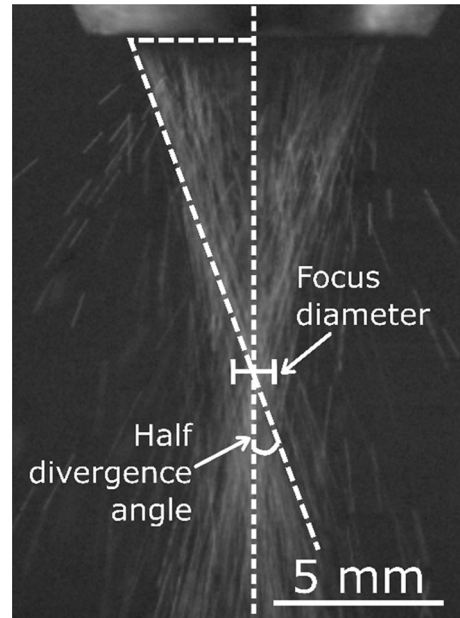


Fig. 2. High-speed camera images of the co-axial powder stream taken at 1000 frames per second (powder mass flow rate = 15 g/min, argon shielding gas flow rate = 16 L/min, and helium carrier gas flow rate = 10 L/min).

**Table II. Process variables investigated**

| Process variables | Variations |
|---|---|
| Laser power (kW) | 1.0, 1.5, 2.5 |
| Powder stream focal offset distance (mm) | 0.2, 0.4, 0.6, 0.8 |
| Laser spot size on the substrate (mm) | 1.0–1.17 mm |
| Laser processing speed (m/min) | 10, 20, 30 |
| Powder mass flow rate (g/min) | 15 |
| Track overlap (%) | 50 |

## Characterization

Each UHSLC-deposited track was cross-sectioned in the direction perpendicular to the rotating direction of the substrate. The cross-section samples were mechanically polished for characterization of the clad layer thickness, the laser penetrated depth, and cracks via optical microscopy with a VHX-5000 digital microscope (KEYENCE Corp.). The clad layer thickness or clad height is defined as the distance between the substrate surface and peak of the clad layer profile.[14] The as-deposited microstructure was analyzed using scanning electron microscopy (SEM) on a JSM-7200F scanning electron microscope (JEOL Ltd.) assisted with energy-dispersive spectroscopy (EDS). The grain morphology, grain size, and secondary dendrite arm spacing (SDAS) were analyzed via the backscattered electron (BSE) imaging mode. The cooling rate ($\dot{T}$, K/s) at which the analyzed microstructure solidified is calculated from Eq. 2 developed by Frenk and Kurz using measured SDAS ($\lambda_2$, $\mu$m) in the as-deposited Stellite® 6 microstructure via high-speed laser cladding at varying processing speeds from 1.67 mm/s to 167 mm/s.[15]

$$\lambda_2 = 32.8 \times \dot{T}^{-1/3} \qquad (2)$$

The as-deposited samples were further analyzed for the chemical mixing of Fe across the clad-substrate interface between the laser penetration zone (LPZ) and the heat-affected zone (HAZ) using EDS. The Vickers hardness testing was performed using a Future-Tech Vickers Hardness Tester FV-700 (Future Tech Corp.) at a load of 100 g for 15 s for each indentation. A series of indentations were placed across the cross-sectioned track, starting near the surface of the clad layer to the substrate with an interval of 50 $\mu$m.

## RESULTS AND DISCUSSION

The elevated powder stream focal position above the substrate in UHSLC indicates that it directly impacts the volume of powder that is heated or partially melted by the laser beam before entering the melt pool (Fig. 1c). The increased distance between the powder stream focus and the substrate is expected to influence the size of the molten pool on the substrate surface and the clad layer thickness after solidification. The results in Fig. 3 reveal that the clad layer thickness increased from

194 ± 9 $\mu$m to 252 ± 13 $\mu$m with increasing distance between powder stream focus and substrate from 0.2 mm to 0.8 mm at the laser energy density of 8.11 J/mm². The same effect was observed at two other laser energy density levels (Fig. 3). The relationship shown in Fig. 3 between the powder stream focus position and clad layer thickness suggests a practical strategy to control the clad layer thickness via changing the powder stream focal position.

The dependence of the clad layer thickness on laser energy density illustrated in Fig. 4 showed two different patterns. The clad layer thickness increased with increasing laser energy density from 3 J/mm² to 9 J/mm² but then decreased with increasing laser energy density from 13 J/mm² to 15 J/mm². The increase from 3 J/mm² to 9 J/mm² can be attributed to more powder particles being heated and melted before entering the melt pool on the substrate surface. The reduction in clad layer thickness for laser energy density from 13 J/mm² to 15 J/mm² could be related to the increased evaporation of powder particles during the laser-powder interaction at such high laser energy densities.[13,16] The absence of clad layer thickness measurements between 9 J/mm² and 13 J/mm² was a product of the combinations of the process variables used for the study. These results generally suggest that an optimal laser energy density exists for a maximum clad layer thickness. Similar dependences of clad layer thickness on laser energy densities from 3 J/mm² to 9 J/mm² can be found in recent literature (Fig. 4), despite different materials being used for deposition.[7,16] Again, this can be a process control strategy for targeted clad thickness in commercial practice.

The cross-sectional image of the deposit has three regions, the clad layer, laser penetrated zone (LPZ), and heat-affected zone (HAZ). An overall microstructure of the clad layer is shown in Fig. 5a. It consists of three tracks deposited with a 50%

track overlap from right to left in Fig. 5a. The 50% track overlap was used throughout the study to increase the area coverage while maintaining a satisfactory surface roughness as compared to the 80% to 90% overlap used in the literature on UHSLC.[7,8,17,18] EDS line scans shown in Fig. 5c reveal that the LPZ has a different composition of Fe, Co, and Cr to that of the clad layer and substrate, suggesting metallurgical bonding between the clad layer and the substrate. Columnar grains are evident in the clad layer with a thin layer of equiaxed grains in the clad surface because of more nucleation events brought by the increased cooling rate. The grain structure became coarser from the left to the right region of the clad layer, opposite to the cladding direction. Interdendritic carbide phases were observed because of segregation, consistent with conventional laser clad cases.[19] The average SDAS is 0.89 ± 0.03 $\mu$m (Fig. 5b), which is about 50% smaller than that in the conventionally clad Stellite® 6 microstructure in a single layer deposit.[19] The cooling rate calculated from Eq. 2 is $4.9 \times 10^4$ K/s, ten times faster than that in conventional LC.[19,20] The carbide particles were found agglomerated because of severe local interdendritic segregation, manifested as dark particles in the lower region of Fig. 5b, close to the central region of the clad layer.

The variation in laser energy density also influences the microstructural developments in the deposited coating. The microstructure deposited at 7.68 J/mm² predominately consists of columnar grains with pockets of equiaxed grains in the top region (Fig. 6a) The columnar microstructure was refined by lowering the laser energy density to 5.12 J/mm², indicated by a higher volume of the equiaxed microstructure and the shortenes columnar grains in Fig. 6b. The microstructural refinement effect can be attributed to the increased cooling rate within a smaller melt pool formed at a lower laser energy density. The decrease in energy
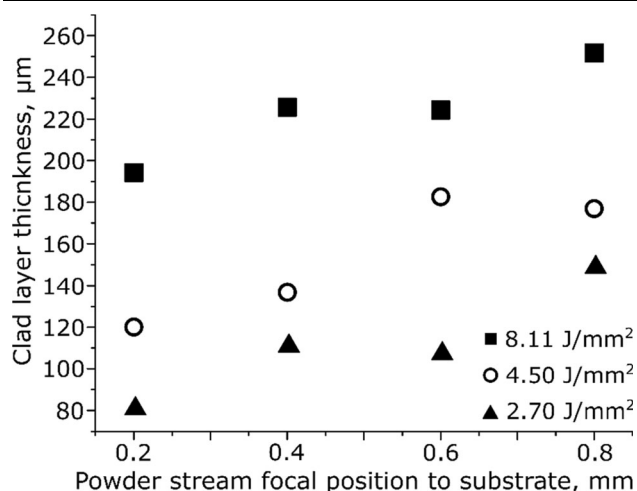


Fig. 3. The relationship between powder stream focal offset and clad layer thickness at three laser energy density levels.
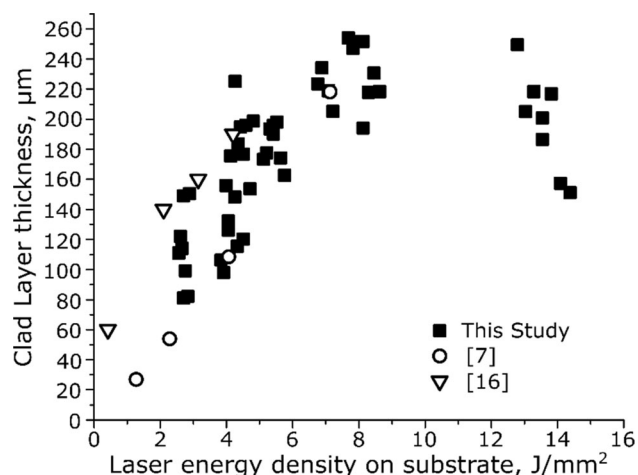


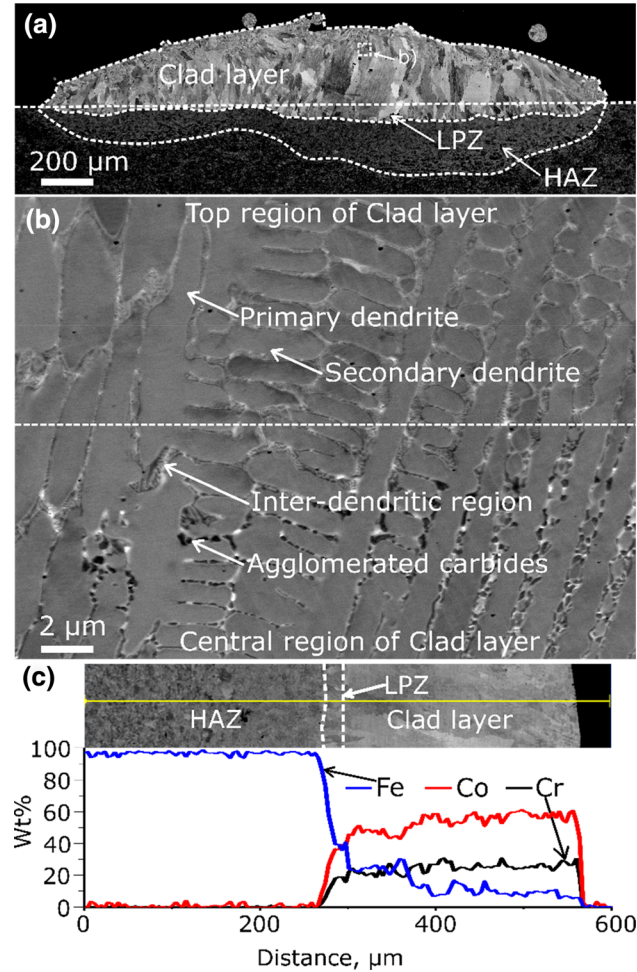Fig. 4. Clad layer thickness versus laser energy density, compared with the literature.[7,16]

Fig. 5. (a) SEM BSE image of the UHSLC deposited tracks at 7.82 J/mm$^2$ ($P$ = 1.5 kW, $V_l$ = 10 m/min, and $D_l$ = 1.15 mm. (b) As-deposited microstructure; (c) EDS line scans from the substrate to the surface of the clad layer.



Fig. 6. SEM BSE images of the UHSLC deposited tracks. (a) At 7.68 J/mm$^2$ with a clad layer thickness of 254 $\mu$m. (b) At 5.12 J/mm$^2$ with a clad layer thickness of 173 $\mu$m. (c) EDS analysis across the interface in (a). (d) EDS analysis across the interface in (b). (e) The microhardness profiles of both deposited tracks.

input also led to a smaller LPZ as there was less laser energy transmitted to the substrate surface after passing through the powder particles. The sample deposited at 5.12 J/mm$^2$ has a shallower laser penetration depth in the substrate, which is confirmed by the EDS profiles shown in Fig. 6d where the Fe concentration decreases rapidly to approximately 3 wt.% after crossing the clad-substrate interface.

The microhardness profiles are similar in both cases (Fig. 6e), and the peak hardness is higher than that observed in conventionally laser clad Stellite® 6,[5,21] which is due to the microstructural refinement effect.[21] The difference in Fe content in the clad layer obtained at different laser energy density levels (Fig. 6c and d) is potentially contributing to the difference in microhardness observed in Fig. 6e. Detailed characterization of the phases present in the clad layer are needed to establish the effects of Fe content on the microhardness of Stellite® 6 deposited by UHSLC.
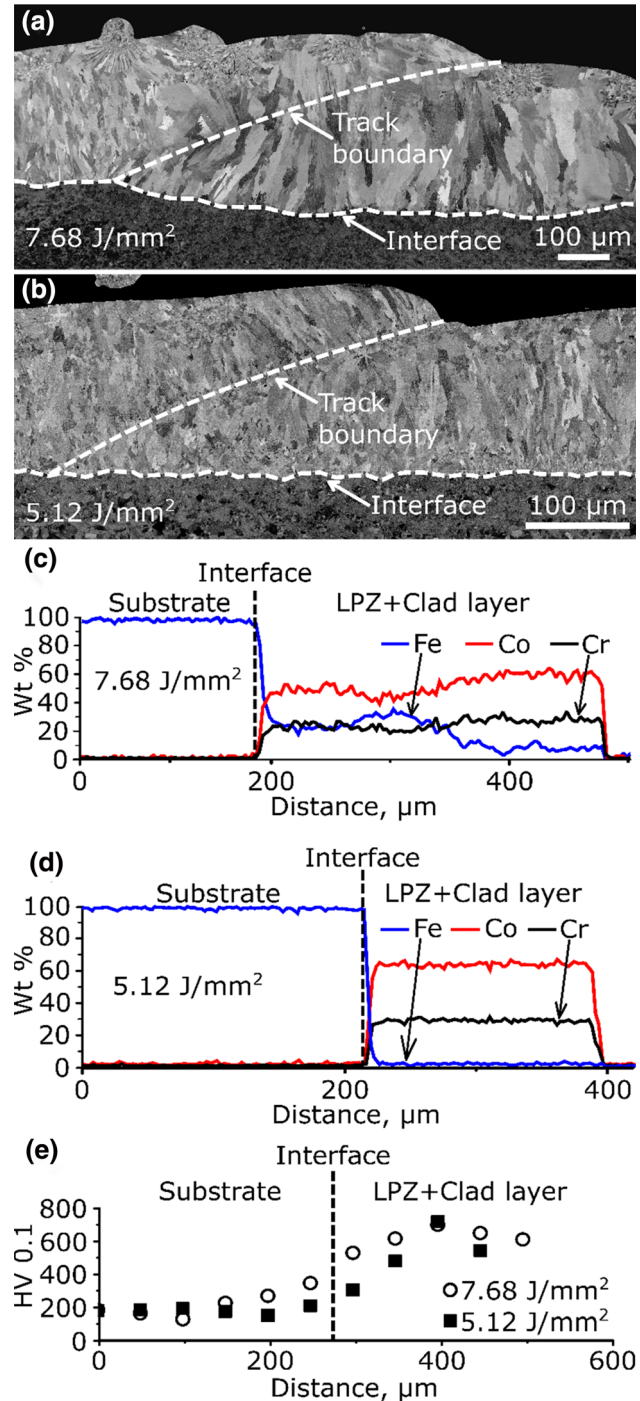
The Stellite® 6 tracks deposited at a laser energy density of 12.79 J/mm$^2$ and above exhibited significant cracking (most likely hot cracking) along the columnar grain boundaries in both the upper and lower regions of the clad sample (Fig. 7a and b), similar to the findings in previous literature regarding conventional LC at high scanning speeds.[22,23]
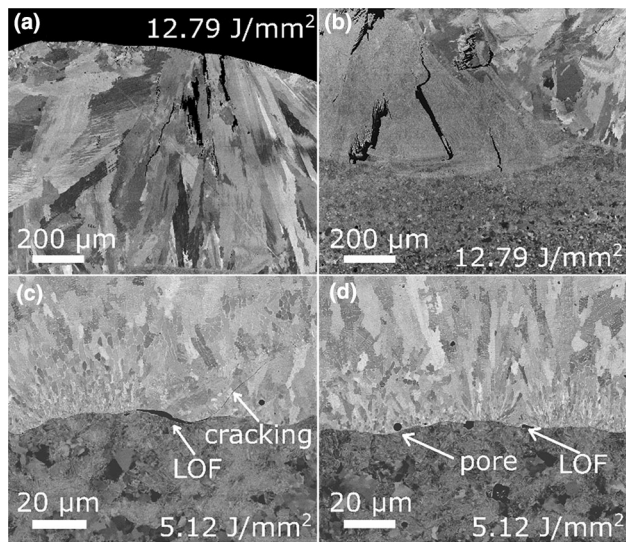
Fig. 7. Defects in UHSLC deposited Stellite® 6 layers with a track overlap of 50%: (a) Cracks propagated to the surface of the clad layer. (b) Cracks originated from the bottom of the LPZ. (c) Lack of fusion and cracks at the clad-substrate interface. (d) Small pore and lack of fusion at the clad-substrate interface.

This can be explained by the following. The use of high laser energy density leads to the formation of a deeper LPZ and excessive mixing of Stellite® 6 and substrate material.[24] It further facilitated the formation of small pores and lack of fusion (LOF) defects in the interdendritic region,[24] from which cracking is most likely originated under high residual thermal stress during rapid solidification according to findings from the literature.[23,24] Reducing the laser energy density leads to a shallower LPZ with less cracking in the clad layer examined. However, lack of fusion defects and small pores are still present at the clad-substrate interface when lowering the laser energy density (Fig. 7c and d). More investigations are required to determine the exact cause of cracking in the as-deposited samples.

## CONCLUSION

We have investigated the influence of the laser energy density (2.56–15.00 J/mm$^2$) and powder stream focus position relative to the substrate (0.2–0.8 mm) on ultra-high-speed laser cladding (UHSLC) of Stellite® 6 powder on mild steel substrates. The following conclusions can be drawn.

- The laser energy density exhibited a dominant influence on the composition, thickness and as-deposited microstructure of the clad layer.
- Increasing the laser energy density from 2.56 J/mm$^2$ to 9.0 J/mm$^2$ increased the layer thickness. Further increases from 12.79 J/mm$^2$ to 15.00 J/mm$^2$ decreased the layer thickness.
- Increasing the distance between the powder stream focus position and the substrate from 0.2 mm to 0.8 mm increased clad layer thickness at constant laser energy density.

- The deposited microstructure consisted of columnar grains growing from the laser penetration zone towards the surface of the clad layer and equiaxed grains at the surface of the clad layer because of the increased solidification rate of the melt pool.
- Significant cracking was found in coatings deposited at laser energy density of 12.79 J/mm$^2$ and higher. The reason can be attributed to the excessive mixing of Stellite® 6 and substrate material and most likely caused by the high residual thermal stress during deposition, which requires confirmation in future studies.

## CONFLICT OF INTEREST

The authors declare that they have no conflict of interest.

## REFERENCES

1. D.S. Gnanamuthu, In *Cladding*, ed. United States Patent (Avco Everett Research Laboratory, Inc., New York, 1976), p. 11.
2. G. Xu, M. Kutsuna, and K. Yamada, *J. Jpn. Weld. Soc.* 23, 286 (2005).
3. D. Gu, *Laser Additive Manufacturing of High-Performance Materials* (Berlin, Heidelberg: Springer, 2015). https://doi.org/10.1007/978-3-662-46089-4_2.
4. W. Küppers, G.M. Backes, and J. Kittel, In *Extreme High-Speed Laser Material Deposition* (DE102011100456B4, 2015), p. 6.
5. A. Dworak, J. Sienicki, P. Koruba, and P. Jurewicz, In *AHS International 74th Annual Conference*, ed. AHS International (Alexandra, VA, 2018), p 6.
6. T. Schopphoven, N. Pirch, S. Mann, R. Poprawe, C.L. Häfner, and J.H. Schleifenbaum, *Coatings* 10, 4 (2020).
7. C. Lampa and I. Smirnov, *J. Laser Appl.* 31, 022511 (2019).
8. F. Shen, W. Tao, L. Li, Y. Zhou, W. Wang, and S. Wang, *Appl. Surf. Sci.* 517, 146085 (2020).
9. L. Li, F. Shen, Y. Zhou, and W. Tao, *J. Laser Appl.* 31, 042009 (2019).
10. D.A. Belforte, *SPIE Proc.* 0270, 66 (1981).
11. T. Schopphoven, A. Gasser, and G. Backes, *Laser Tech. J.* 14, 26 (2017).
12. M.J. Troughton, *Handbook of Plastics Joining*, ed. M.J. Troughton (Boston: William Andrew Publishing, 2009), pp. 81–95.
13. S.M. Thompson, L. Bian, N. Shamsaei, and A. Yadollahi, *Addit. Manuf.* 8, 36 (2015).
14. E. Toyserkani, A. Khajepour, and S.F. Corbin, *Laser Cladding* (Boca Raton: CRC Press, 2005), pp. 23–40.
15. A. Frenk and W. Kurz, *Mater. Sci. Eng. A* 173, 339 (1993).
16. T. Schopphoven, A. Gasser, K. Wissenbach, and R. Poprawe, *J. Laser Appl.* 28, 022501 (2016).
17. D. Ding, Z. Pan, D. Cuiuri, and H. Li, *Robot. CIM-INT Manuf.* 31, 101 (2015).
18. Y.X. Li and J. Ma, *Surf. Coat. Technol.* 90, 1 (1997).

19. S. Sun, Y. Durandet, and M. Brandt, *Surf. Coat. Technol.* 194, 225 (2005).
20. S. Sun and M. Brandt, In *ICALEO*, p. 901 (2004).
21. M. Furukawa, Z. Horita, M. Nemoto, R.Z. Valiev, and T.G. Langdon, *Acta Mater.* 44, 4619 (1996).
22. K. Partes, T. Seefeld, G. Sepold and F. Vollertsen, In *ICALEO*, pp. 621–628 (2005).
23. K. Partes and G. Sepold, *J. Mater. Process Technol.* 195, 27 (2008).
24. C. Barr, S. Da Sun, M. Easton, N. Orchowski, N. Matthews, and M. Brandt, *Surf. Coat. Technol.* 340, 126 (2018).